nature astronomy

LETTERS

https://doi.org/10.1038/s41550-019-0978-6

The partitioning of the inner and outer Solar System by a structured protoplanetary disk

R. Brasser[1] and S. J. Mojzsis[2,3]

Mass-independent isotopic anomalies define two cosmochemically distinct regions: the carbonaceous and non-carbonaceous meteorites[1], implying that the non-carbonaceous (terrestrial) and carbonaceous (Jovian) reservoirs were kept separate during and after planet formation. The formation of Jupiter is widely invoked to explain this compositional dichotomy by acting as an effective barrier between the two reservoirs[2]. Jupiter's solid kernel possibly grew to 20 Earth masses ($M_\oplus$) in 1 Myr from the accretion of submetre-sized objects ('pebbles'), followed by slower accretion via planetesimals. Subsequent gas envelope contraction led to Jupiter's formation as a gas giant[3]. Here, we use dynamical simulations to show that the growth of Jupiter from pebble accretion is not fast enough to be responsible for the inferred separation of the terrestrial and Jovian reservoirs. We propose instead that the dichotomy was caused by a pressure maximum in the disk near Jupiter's location, which created a ringed structure such as those detected by ALMA[4]. One or multiple such—potentially mobile—long-lived pressure maxima almost completely prevented pebbles from the Jovian region reaching the terrestrial zone, maintaining a compositional partition between the two regions. We thus suggest that our young Solar System's protoplanetary disk developed at least one and probably multiple rings, which potentially triggered the formation of the giant planets.

We have numerically modelled the combined growth of Mars and Jupiter via dynamical simulations of pebble and gas envelope accretion (see Methods) to establish whether the growing Jupiter presents a powerful enough barrier to create the observed compositional dichotomy. In our adopted model, pebbles that joined together to produce the solid kernels of the giant planets are thought to have originated as coagulants in the outer regions of the protoplanetary disk and subsequently spiralled towards the Sun due to gas drag[5]. During the swift growth of Jupiter's solid kernel, pebbles may reach the inner Solar System, but once the kernel attains its pebble isolation mass of around $20\,M_\oplus$ (ref. [6]), the pebble flux to the inner Solar System ceases. For a nominal pebble flux, $\dot{M}_\mathrm{p}$, of $10^{-4}\,M_\oplus\mathrm{yr}^{-1}$ (refs. [6,7]) and typical protoplanetary disk parameters[5,7] (see Methods), the efficiency of accreting pebbles by the growing Jupiter in our model is approximately[7,8]

$$f = 3\%\left(\frac{\mathcal{S}}{0.1}\right)^{-1/3}\left(\frac{r}{1\,\mathrm{au}}\right)^{-4/7}\left(\frac{M}{0.1\,M_\oplus}\right)^{2/3} \quad (1)$$

for planet masses, $M, \gtrsim 0.1\,M_\oplus$, and

$$f = 3\%\left(\frac{\mathcal{S}}{0.1}\right)^{1/2}\left(\frac{r}{1\,\mathrm{au}}\right)^{-6/7}\left(\frac{M}{0.1\,M_\oplus}\right) \quad (2)$$

for $M \lesssim 0.1\,M_\oplus$. Here, $\mathcal{S}$ is the Stokes number of the drifting pebbles (a measure of how strong the pebbles are coupled to the gas) and r is the distance to the Sun. The pebble accretion efficiency decreases with increasing heliocentric distance. In our model, the radii of the pebbles are calculated self-consistently and depend on the disk parameters (see Methods). At Jupiter's orbit, the pebble radius is ~40 cm, so that $\mathcal{S} \approx 0.1$ (ref. [7]) and the mass-doubling timescale

$$t_\mathrm{acc} = \frac{M\ln 2}{\dot{M}_\mathrm{p} f} \quad (3)$$

is ~0.07 Myr for a nominal pebble flux. It thus takes ~1 Myr to grow Jupiter's kernel from $<0.01\,M_\oplus$ to the requisite $20\,M_\oplus$, in agreement with cosmochemical age constraints[2]; a potentially lower pebble isolation mass of $10\,M_\oplus$ marginally decreases this accretion time. For the first ~0.8 Myr, our adopted model shows that >50% of the pebbles spiral past the developing Jupiter and thus affect the composition of any material interior to it. Therefore, unless there is a substantial reduction in pebble size or mass flux (or both) between Jupiter and Mars, in 1 Myr, a ~1,000 km-diameter planetesimal at 1.5 au could become more massive than Earth due to incorporation of Jovian reservoir material. The total mass of pebbles in the disk is expected to be $\sim 100\,M_\oplus$ (for example, ref. [9]). The low accretion efficiency implies that a comparable pebble mass will reach the 'snow line', or the location where water ice sublimates (usually placed sunwards of Jupiter's orbit). Pebble sublimation at the snow line most likely breaks them into much smaller particles, probably ranging from micrometre- to millimetre-sized grains[10], which reduces the Stokes number to $\lesssim 10^{-3}$ and increases the mass-doubling timescale to ~0.7 Myr for small objects near 1 au. As a result, the expected amount of Jovian reservoir material accreted by planetesimals in the inner Solar System depends strongly on the temporal evolution of the snow line[10] and the original planetesimal size.

We tested this hypothesis using dynamical simulations with the *N*-body code SyMBA (Symplectic Massive Body Algorithm)[11], which was modified to include pebble and gas accretion and planet migration[12] (see Methods). We grew Jupiter to its current mass, beginning with a lunar-mass 'seed' planetary embryo that formed 0.5 Myr after calcium–aluminium-rich inclusions (CAIs). This embryo becomes a $20\,M_\oplus$ kernel 1 Myr later when using a nominal pebble flux; ensuing gas envelope accretion grows Jupiter to $320\,M_\oplus$ after another 2 Myr (Fig. 1), just before the dispersal of the protoplanetary disk[13]. We placed a second planetary seed at 1.5 au with initial masses of $10^{-4}\,M_\oplus$, $10^{-3}\,M_\oplus$ or $10^{-2}\,M_\oplus$. The initial disk temperature at 1 au was varied from 200 K to 300 K, and we used a mass sublimation fraction of 50% at the snow line[10,12]. We kept

[1]Earth Life Science Institute, Tokyo Institute of Technology, Tokyo, Japan. [2]Department of Geological Sciences, University of Colorado Boulder, Boulder, CO, United States. [3]Institute for Geological and Geochemical Research, Research Centre for Astronomy and Earth Sciences, Hungarian Academy of Sciences, Budapest, Hungary. e-mail: brasser_astro@yahoo.com; stephen.mojzsis@colorado.edu

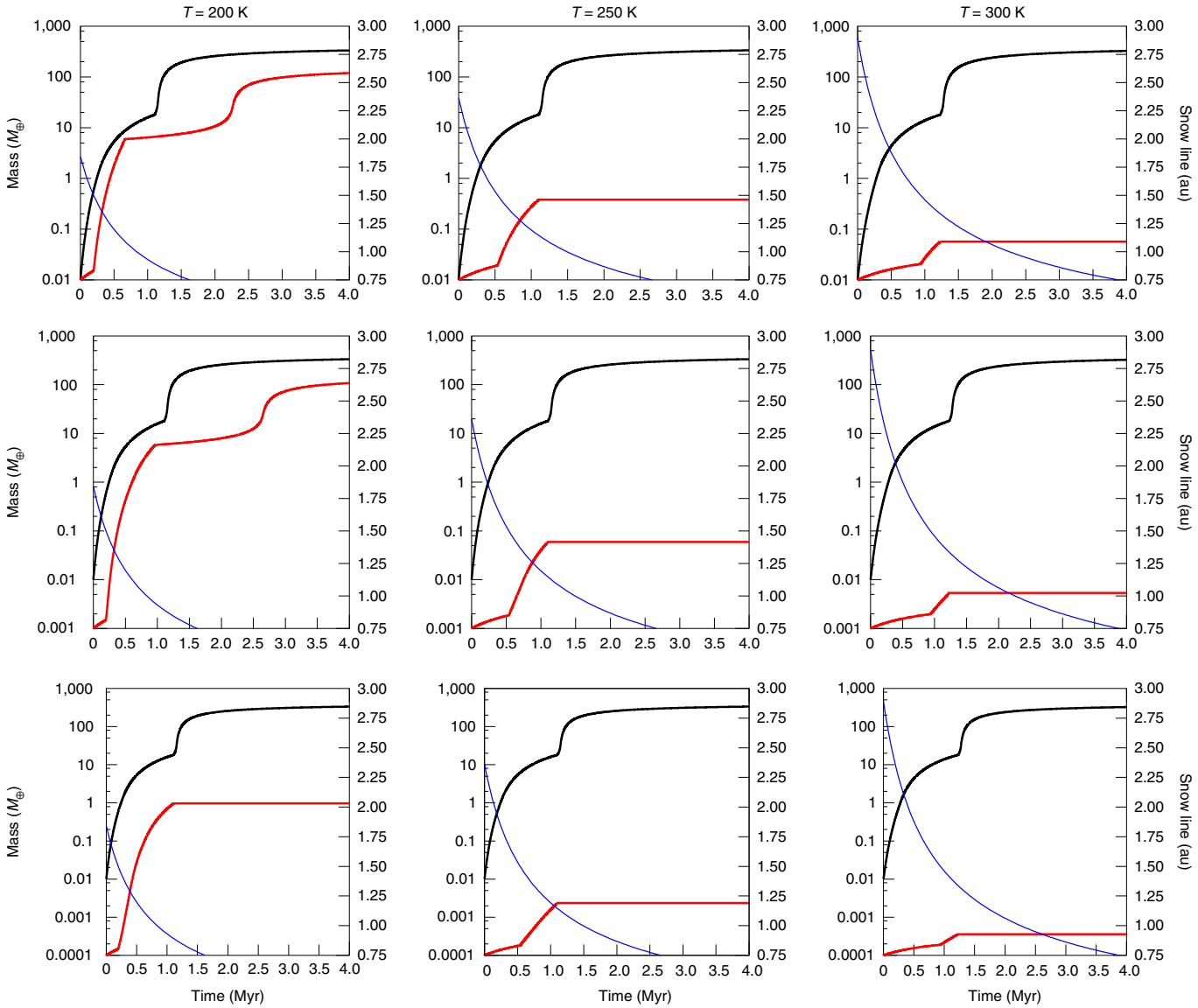

Fig. 1 | Evolution of the mass of Jupiter and a Mars analogue as a function of time when growing by pebble accretion. The black line denotes Jupiter, the red line Mars and the blue line denotes the location of the snow line in astronomical units (right axis). The columns show temperature, *T*, variations and the rows the initial mass of the Martian embryo. The kinks in the growth curve for Mars near 0.5–1 Myr are caused by the snow line crossing the Martian embryo. This causes the Stokes number of the pebbles to increase and with it the accretion rate. The second kink near 1–1.5 Myr is caused by Jupiter reaching the pebble isolation mass, which shuts off the pebble flow to the Martian embryo. In the top left panels, Mars's increased growth is the result of runaway gas envelope accretion.

the planets in place to focus on their mass evolution; the migration timescale becomes comparable to the pebble accretion timescale only when $M \gtrsim 0.1\,M_\oplus$, so that growth usually dominates migration, and migrating planets may not reach their pebble isolation mass before they have arrived at the star[14].

The best combination of parameters that yields a Mars-sized planet at 1.5 au has an initial mass of $10^{-3}\,M_\oplus$ and gas temperature of 250 K at 1 au (Fig. 1); all other cases produce Mars analogues that are either extremely large ($>1\,M_\oplus$) or extremely small ($<0.03\,M_\oplus$). As expected, the final mass of the Mars analogue sensitively depends on both its initial seed mass and when the snow line crosses the Martian embryo: too early leads to rapid accretion of volatile-rich pebbles ($\mathcal{S} \approx 0.1$; $t_{\rm acc} \approx 0.07$ Myr), whereas too late means that the seed embryo barely grows at all ($\mathcal{S} \approx 10^{-4}$; $t_{\rm acc} \approx 0.7$ Myr). Various additional simulations of the same parameter space that begin with only multiple seed embryos, or with only a swarm of planetesimals spread out over the same range, confirm this conclusion (Fig. 2). Therefore, small planetesimals that are initially closer than 1.5 au roughly double their masses in 1 Myr; large planetesimals and seed embryos can accrete much more, possibly up to the pebble isolation mass[6], depending on the evolution of the snow line. Other sensitivity tests, such as changing the stellar accretion rate, accounting for planet migration of the embryos and Jupiter, or altering the disk temperature and initial mass of embryos (or planetesimals) change the dynamical outcome of the simulations, but not the overall composition (see Extended Data Figs. 1–4).

When we take the carbonaceous chondrite meteorites as a proxy for Jovian reservoir material[1], an embryo with an initial mass of $10^{-3}\,M_\oplus$ at 1.5 au will not have the same composition as Mars. Hence, this scenario poses a problem for the documented composition of inner Solar System bodies. Nucleosynthetic isotopic variations of oxygen (O), titanium (Ti), chromium (Cr) and nickel (Ni)

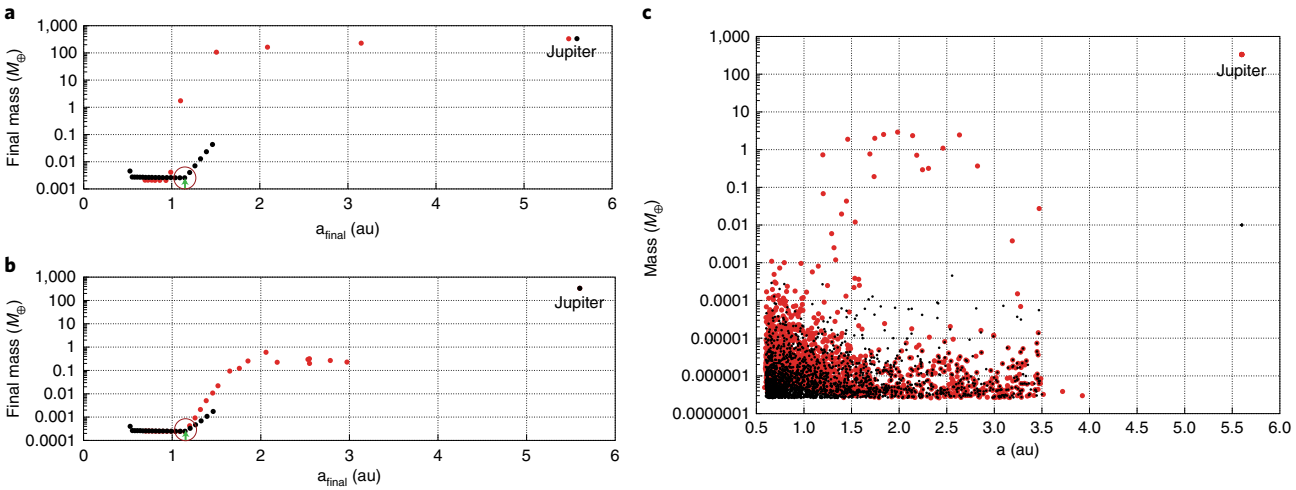

Fig. 2 | Outcome of pebble accretion simulations with embryos or planetesimals. a,**b**, Final masses and semi-major axes of pebble accretion simulations from multiple planetary seed embryos with initial masses of $10^{-3}\,M_\oplus$ (**a**) and $10^{-4}\,M_\oplus$ (**b**). The red dots are for runs where the embryos are initially placed from 0.5 au to 3.5 au, and black dots have embryos from 0.5 au to 1.5 au. Green arrows and red circles indicate the location of the snow line when Jupiter shuts off the pebble flow. When there are embryos in the asteroid belt, we can produce gas giants (**a**) or Mars-sized planets in this region. When the disk is truncated, we can obtain a Mars analogue at 1.5 au (**b**). **c**, Initial (black) and final (red) masses and semi-major axes of a swarm of planetesimals with initial diameters from 100 km to 2,000 km with a cumulative size-frequency distribution of $N(>D) \propto D^{-5/2}$ (ref. [6]) and initial density of 2,000 kg m^{-3}; this is a top-heavy distribution where most of the mass is in the large bodies. The initial disk temperature at 1 au was 200 K. In the innermost portion of the planetesimal disk, bodies accrete >50% of their own mass in pebbles. The growth is inside out[7].

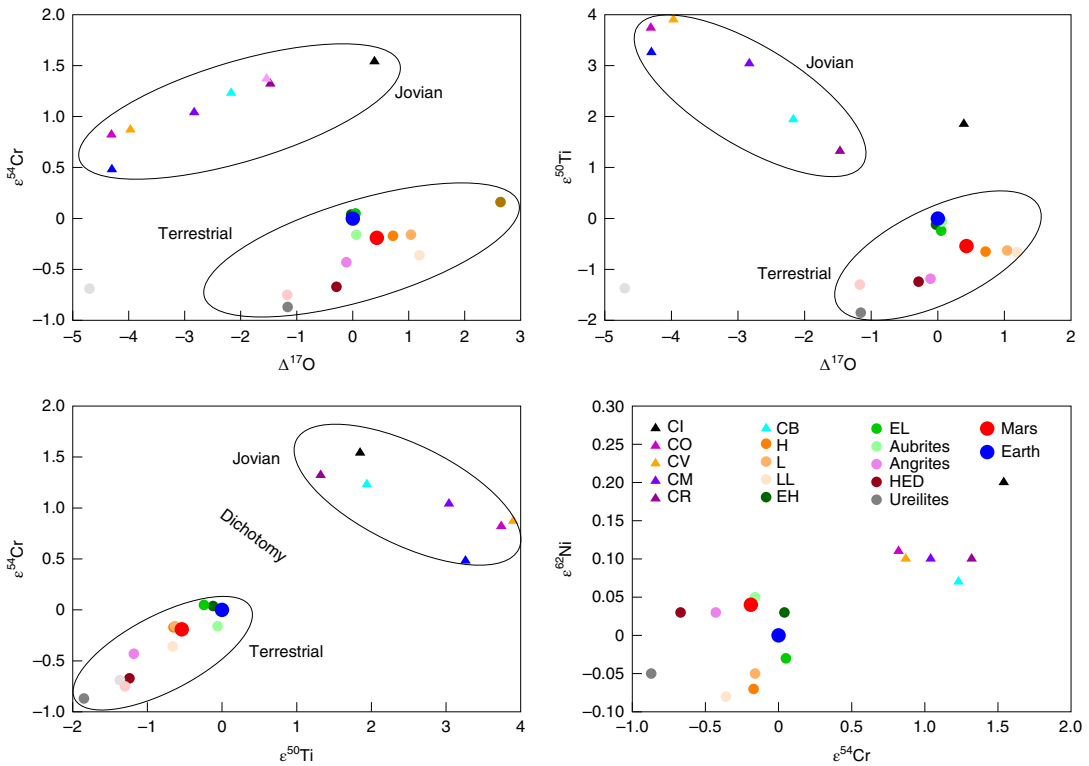

Fig. 3 | Mean isotopic anomalies for several major groups of meteorites, Earth and Mars. Mean isotopic anomalies in O versus Ti (top right), O versus Cr (top left), Ti versus Cr (bottom left) and Cr versus Ni (bottom right). The trends for non-carbonaceous and carbonaceous materials, where they exist, are shown with solid lines. Carbonaceous/Jovian materials are shown with triangles, and non-carbonaceous/terrestrial materials are shown with filled circles. Earth and Mars are made larger for clarity. The dichotomy between the carbonaceous and non-carbonaceous reservoirs is immediately obvious, not only in their separation, but also in their different behaviour. Earth is an endmember in ε^{50}Ti versus ε^{54}Cr space and shows an offset from the non-carbonaceous material in Δ^{17}O versus ε^{50}Ti space, indicating possible pollution by Jovian reservoir materials. The data are compiled from the literature sources listed in Methods. $\varepsilon^{54}\mathrm{Cr} = [(^{54}\mathrm{Cr}/^{52}\mathrm{Cr})_{sample}/(^{54}\mathrm{Cr}/^{52}\mathrm{Cr})_{standard} - 1] \times 10^4$. $\varepsilon^{50}\mathrm{Ti} = [(^{50}\mathrm{Ti}/^{48}\mathrm{Ti})_{sample}/(^{50}\mathrm{Ti}/^{48}\mathrm{Ti})_{standard} - 1] \times 10^4$. $\varepsilon^{62}\mathrm{Ni} = [(^{62}\mathrm{Ni}/^{61}\mathrm{Ni})_{sample}/(^{62}\mathrm{Ni}/^{61}\mathrm{Ni})_{standard} - 1] \times 10^4$. $\Delta^{17}\mathrm{O} = \delta^{17}\mathrm{O} - 0.52\delta^{18}\mathrm{O}$. CI, CO, CV, CM, CR and CB are the various carbonaceous chondrites; H, L and LL are the ordinary chondrite group; EH and EL are the enstatite chondrite group. Some panels include the R chondrites and CH carbonaceous chondrites.

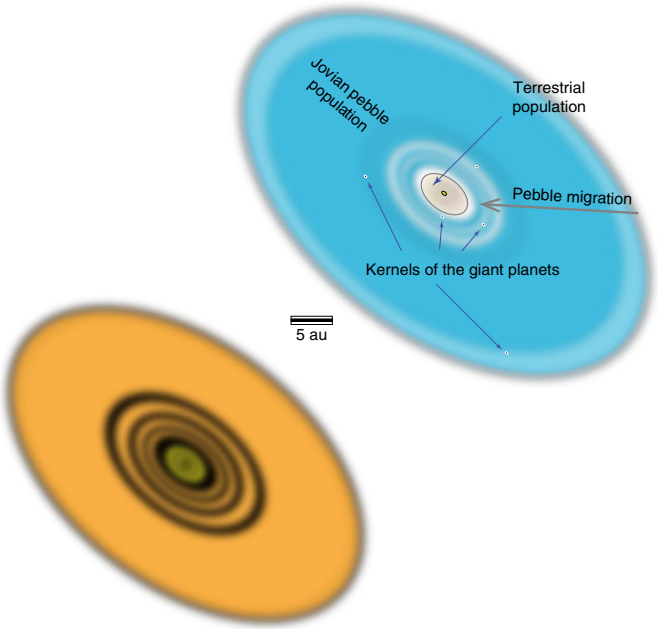

Fig. 4 | Schematic illustration of the protoplanetary disk structure of the infant Solar System and the possible formation locations of the giant planets. How the rings may appear in an ALMA image (left) and the location of the various pebble populations, rings and kernels of the giant planets (right). Here, the rings are situated between 5 au and 30 au, although they could originally have been farther away if they migrated towards the star together with the giant planets. Here, we do not assume that the giant planets formed in a multi-resonant configuration.

measured from Martian meteorites indicate that Mars should not have accreted more than a few per cent of its mass with Jovian reservoir materials[15]. Even if Mars ultimately formed through multiple collisions of planetesimals or seed embryos rather than solely by pebble accretion[16], the conundrum that arises in the scenario provided herein is that such bodies will have roughly doubled their initial masses through pebble accretion by the time Jupiter shuts off the pebble flow before coagulating into Mars. The same arguments apply to the other terrestrial planets, or in the event that planetesimals formed even earlier than explored in this work[2] (see Extended Data Figs. 1–4). Consequently, the formation of Jupiter's kernel over 1 Myr through pebble accretion cannot be responsible for the effective separation of the Jovian and terrestrial reservoirs.

Isotopic data further indicate that Earth is an endmember of our existing sample suite of non-carbonaceous (terrestrial) material in ε^{50}Ti versus ε^{54}Cr space, and that Earth and Mars appear to form a continuation of the carbonaceous (Jovian) material in Δ^{17}O versus ε^{50}Ti space (Fig. 3). However, a small leakage of pebbles from the Jovian reservoir can account for the observed trend. Indeed, estimates from nitrogen and hydrogen isotopes from Earth's volatile budget imply a 2% Jovian material contribution by mass[17], whereas mixing models that reproduce the isotopic signatures of Earth and Mars from various groups of primitive meteorites point to a higher contribution of 3–10% by mass[18]. The incorporation of Jovian material is thought to have occurred relatively early in the planets' accretion histories[18].

A plausible mechanism to effectively separate the two reservoirs, and stem the pebble flux to the inner Solar System, is a radial midplane pressure profile with ring-like pressure maxima that are intrinsic to the Solar System's protoplanetary disk. Observations by the ALMA (Atacama Large Millimetre/submillimetre Array) observatory of protoplanetary disks around young stars show that dust trapping is ubiquitous, leading to a rich variety of ring structures and annuli[4], the origins of which are still debated[19–21]. Even though planet formation mechanisms have been employed to explain the ringed appearance of the disks (for example, ref. [21]), our study suggests that non-planet-related mechanisms may be at work. Pressure maxima in such disks result in dust grains piling up near these maxima, creating a bright ring; pressure increases of 25% are sufficient to produce the dust concentrations observable with ALMA[22]. Dust grains at the pressure minima are rapidly depleted[23,24], manifesting as a dark ring. A long-lived structure in the protosolar disk near Jupiter that formed before the planet, or such an initially distant and mobile structure that moved sunwards to 5 au, coupled with a disk wind that removes mass from the inner disk[24], can explain the separation between carbonaceous and non-carbonaceous materials (Fig. 4). This structure could further explain the low mass of the asteroid belt region due to dust depletion, and serves to prevent Jupiter from migrating much closer to the Sun. A small amount of turbulent diffusion through the ring can account for the apparent contamination of the terrestrial reservoir (in particular, Earth) by the Jovian reservoir (Fig. 3).

Evidence for such diffusion may come from the parent bodies of several achondrite meteorite groups. The HED (howardite–eucrite–diogenite), angrite and ureilite parent bodies are thought to have all been roughly the same size[25]. The ureilite parent body may have formed near 2.8 au, farther than 4 Vesta's current orbit[25]; isotopic data suggest that the angrite parent body could have formed near Vesta[25] and that the seed embryos for Mars and Earth all coalesced progressively closer in. This observed cosmochemical trend is expected: our model predicts that a lower amount of Jovian reservoir material is accreted with increasing heliocentric distance[7,10] (Fig. 2).

We advocate for the existence of at least one ring in the nascent Solar System's outer protoplanetary disk near 5 au (ref. [26]) and that Jupiter formed near this ring. Additional rings could lead to the formation of the other giant planets, each with a kernel mass of 15 $M_\oplus$. Distinct annuli in ALMA disks may thus point to the presence of (forming) distant giant planets, whereas those without such substructures could have a dearth of giant-planet kernels. For example, observations of such rings in the Taurus star-forming region show that the gaps and rings are spaced such that the distance of a ring to the star, $R_{\rm ring}$, versus that of a gap, $R_{\rm gap}$, scales as $R_{\rm ring}/R_{\rm gap} \approx 1.1–1.3$ (ref. [27]), which brackets the 3/2 and 2/1 resonances between two rings; such a spacing is consistent with the preferred initial configuration of the giant planets in the Solar System[28]. With a single ring, however, the initial mutual spacing of the forming giant planets becomes less well constrained[29]. In our pebble accretion model, the solid kernels of Jupiter and Saturn grow much faster than those of Uranus and Neptune (see Extended Data Fig. 3). With multiple rings, the individual growth timescale of each kernel becomes less clear. In a ringed disk, the kernels of these planets probably grew mostly from locally formed pebbles[30] in the Jovian reservoir. Pebbles and dust particles generally pile up at each pressure maximum[24], so that only a few per cent of Jovian material reached the inner Solar System. If the different isotopic compositions of the various carbonaceous chondrites reflect to some degree their formation location, then our hypothesis further predicts that the isotopic compositions of the giant planets are distinct from one another and more closely resemble carbonaceous chondrites than any inner Solar System object.

Methods

Our methodology is based almost entirely on that of ref. [7] as implemented in ref. [12].

Disk model. We assume a steady accretion rate of the disk gas onto the Sun. The gas accretion rate, $\dot{M}_\star$, is a function of the gas surface density, Σ, and disk scale height, H, via

$$\dot{M}_\star = 3\pi\alpha\Sigma H^2\Omega_{\rm K} \quad (4)$$

where $\Omega_{\rm K}$ is the orbital frequency. The α-viscosity $\alpha = \nu/(c_s^2\Omega_{\rm K})$ is assumed to be constant[31]; its nominal value is set to 10^{-3} and ν is the viscosity of the gas. This prescription yields a gas surface density that is comparable to the minimum mass solar nebula; we did not consider other values of α at this time. The disk scale

height is related to the temperature, T, and the sound speed, c_s, via $H = c_s/\Omega_K$, where $c_s = (\gamma k_B T/\mu m_p)$. Here, $\gamma = 7/5$ is the ratio of specific heats, k_B is the Boltzmann constant, m_p is the mass of the proton, and $\mu = 2.3$ is the mean atomic mass of the gas. The quantity $\dot{M}_\star$ decreases with time according to[32]

$$\log\left(\frac{\dot{M}_\star}{M_\odot\ \mathrm{yr}^{-1}}\right) = -8 - \frac{7}{5}\log\left(\frac{t}{1\ \mathrm{Myr}} + 0.1\right) \quad (5)$$

where $M_\odot$ is solar masses, and the extra 0.1 Myr is added to avoid the logarithmic singularity.

The disk midplane temperature is $T = \max(T_{vis}, T_{irr})$, where T_{vis} and T_{irr} are temperatures determined by viscous heating and stellar irradiation, respectively. Close to the star, viscous heating dominates; stellar irradiation is the main heating source far away. The detailed disk models of ref. [33] with constant opacity are empirically fitted by

$$\begin{aligned} T_{vis} &= T_{0v}\alpha_3^{-1/5}\dot{M}_{\star 8}^{2/5}\left(\frac{r}{1\ \mathrm{au}}\right)^{-9/10}\ \mathrm{K} \\ T_{irr} &= 150\left(\frac{r}{1\ \mathrm{au}}\right)^{-3/7}\ \mathrm{K} \end{aligned} \quad (6)$$

where the power exponents are derived analytically and T_{0v} is the initial temperature at 1 au. We also define

$$\alpha_3 \equiv \frac{\alpha}{10^{-3}} \quad (7)$$

$$\dot{M}_{\star 8} \equiv \frac{\dot{M}_\star}{10^{-8}\ M_\odot\ \mathrm{yr}^{-1}} \quad (8)$$

With this prescription, we compute the reduced gas scale height $h = H/r$ as

$$\begin{aligned} h_{vis} &= 0.034\left(\frac{T_{0v}}{200\ \mathrm{K}}\right)^{1/2}\alpha_3^{-1/10}\dot{M}_{\star 8}^{1/5}\left(\frac{r}{1\ \mathrm{au}}\right)^{1/20} \\ h_{irr} &= 0.029\left(\frac{r}{1\ \mathrm{au}}\right)^{2/7} \end{aligned} \quad (9)$$

The actual reduced scale height is given by $h = \max(h_{vis}, h_{irr})$, where h_{vis} and h_{irr} are the reduced scale heights determined by viscous heating and stellar irradiation, respectively. Thus, the disk flares in the irradiative region, but not in the viscous region. Equations (4), (6) and (9) may be combined to compute the surface density of the gas determined by viscous heating and stellar irradiation, which are, respectively

$$\begin{aligned} \Sigma_{vis} &= 1,320\left(\frac{T_{0v}}{200\ \mathrm{K}}\right)^{-1}\alpha_3^{-4/5}\dot{M}_{\star 8}^{3/5}\left(\frac{r}{1\ \mathrm{au}}\right)^{-3/5}\ \mathrm{g\,cm^{-2}} \\ \Sigma_{irr} &= 1,785\alpha_3^{-1}\dot{M}_{\star 8}\left(\frac{r}{1\ \mathrm{au}}\right)^{-15/14}\ \mathrm{g\,cm^{-2}} \end{aligned} \quad (10)$$

The boundary between the viscous and irradiation regimes occurs when $T_{vis} = T_{irr}$, that is,

$$r_{vis/irr} = \left(\frac{T_{0v}}{150\ \mathrm{K}}\right)^{70/33}\alpha_3^{-14/33}\dot{M}_{\star 8}^{28/33} \approx 1.84\alpha_3^{-14/33}\dot{M}_{\star 8}^{28/33}\ \mathrm{au} \quad (11)$$

Volatiles inside pebbles should sublimate at the snow line (defined by the distance at which $T \approx 170$ K). Therefore, the size of pebbles and properties of pebble accretion should change at the snow line. Its location is at $r_{snow} = \max[(T_{0v}/170\ \mathrm{K})^{10/9}\alpha_3^{-2/9}\dot{M}_{\star 8}^{4/9}, 0.75] \approx \max[1.2\alpha_3^{-2/9}\dot{M}_{\star 8}^{4/9}, 0.75]$au.

Pebble accretion. The pebble accretion rate onto a planetary embryo is given by

$$\dot{m} = \min\left[1, \frac{C\chi b^2}{4\sqrt{2\pi}\mathcal{S}h_p\zeta}\left(1 + \frac{3b}{2\chi\eta}\right)\right]\dot{M}_F \quad (12)$$

where C is a coefficient, h_p is the reduced pebble scale height (see equation 17 below) and b is the normalized radius of cross-section for accretion (see equation 18 below). The parameters ζ and χ are functions of the Stokes number, and are given by

$$\zeta = \frac{1}{1 + \mathcal{S}^2} \quad (13)$$

$$\chi = \zeta\sqrt{1 + 4\mathcal{S}^2} \quad (14)$$

The fundamental quantity that determines the pebble accretion rate is the mass flux of pebbles through the disk, $\dot{M}_F$. There are several ways to parametrize this quantity, the most popular one relying on the growth of grains in the disk[7]. With this prescription, we obtain

$$\dot{M}_F = 9\times 10^{-4}\mathcal{F}\alpha_3^{-1}\dot{M}_8\left(\frac{t}{1\ \mathrm{Myr}}\right)^{-1/3} M_\oplus\ \mathrm{yr}^{-1} \quad (15)$$

where $\mathcal{F}$ is a factor that accounts for imperfect pebble accretion. When $t > 1$ Myr, the location in the disk where the pebbles form, that is the pebble front, has reached the presumed outer edge of the disk, and we provide an exponential taper of the form $\exp(-t/0.2\ \mathrm{Myr})$ to slow down the pebble flux at later times (ref. [7]). For low-mass objects, pebble accretion happens in three dimensions because the Hill radius of the objects is much smaller than the scale height of pebbles as they migrate through the disk. At higher masses, however, the accretion becomes two-dimensional. The type of accretion is determined by the constant C, given by

$$C = \min\left(\sqrt{\frac{8}{\pi}}\frac{h_p}{b}, 1\right) \quad (16)$$

where the two terms in parentheses correspond to two- and three-dimensional regimes, respectively. In the above equation, h_p is related to the reduced gas scale height through

$$h_p = \left(1 + \frac{\mathcal{S}}{\alpha}\right)^{-1/2} h \quad (17)$$

Since generally $\alpha \ll 1$, we have $h_p \approx \alpha^{-1/2}h$. The quantity b is given by

$$b = 2\kappa r_H \mathcal{S}^{1/3}\min\left(\sqrt{\frac{3r_H}{\chi\eta}}\mathcal{S}^{1/6}, 1\right) \quad (18)$$

where κ is a reduction factor (see equation 25 below), η quantifies the difference between the gas and Keplerian velocities due to the gas pressure (P) gradient, and the two terms in parentheses correspond to Bondi and Hill accretion regimes, respectively. In the Bondi regime, the relative velocity between the embryo and a pebble is dominated by a pebble's drift velocity, whereas in the Hill regime, it is dominated by Keplerian shear; two-dimensional accretion always takes place in the Hill regime. In the above equation, $r_H = (M/3M_\odot)^{1/3}$. The parameter η is given by

$$\eta = \frac{h^2}{2}\left|\frac{\mathrm{d}\ln P}{\mathrm{d}\ln r}\right| = \left(3 - \frac{1}{2}q\right)h^2 \quad (19)$$

where $q = -\partial\ln T/\partial\ln r$. In the viscous regime, usually closer than ~2 au, $q = 9/10$, while in the irradiative region, $q = 3/7$.

The Stokes number, $\mathcal{S}$, determines the pebbles' drift rate and accretion efficiency onto the planets. It is defined as[7]

$$\mathcal{S} = \frac{\rho_p r_p}{\rho_g h}\max\left(1, \frac{4r_p}{9\lambda}\right) \quad (20)$$

where ρ_p and r_p are the bulk density and physical radius of a pebble, respectively, ρ_g is the gas midplane density and λ is the mean free path. The midplane gas density is related to the surface density and scale height via

$$\Sigma = \sqrt{2\pi}H\rho_g \quad (21)$$

and the mean free path is

$$\lambda = \frac{\mu m_H}{\rho_g\sigma} \quad (22)$$

where σ is the collision cross-section and m_H is the mass of the hydrogen molecule.

The radius of the pebbles is determined by the location at which they form. There exist two drag regimes in the disk: the Epstein regime and the Stokes regime. In the Epstein regime, which occurs far from the star, pebbles migrate inwards without growth, that is, growth dominates over migration and pebbles grow in situ. In the Stokes regime, which occurs much closer to the star, pebbles migrate without substantial growth. The transition between the two drag regimes occurs at a distance

$$r_{ES} = 2.9\alpha_3^{-21/52}\dot{M}_{\star 8}^{21/52}\dot{M}_{F4}^{7/52}\rho_p^{-7/26}\ \mathrm{au} \quad (23)$$

where $\dot{M}_{F4} = \dot{M}_F/(10^{-4}\ M_\oplus\ \mathrm{yr}^{-1})$. The radii of pebbles in both regimes are then

$$\begin{aligned} r_p &\simeq 87\alpha_3^{-1/2}\dot{M}_{\star 8}^{1/2}\dot{M}_{F4}^{1/2}\rho_p^{-1}\left(\frac{r}{1\ \mathrm{au}}\right)^{-19/14}\ \mathrm{cm} \quad \text{(Epstein)} \\ r_p &\simeq 21\alpha_3^{5/104}\dot{M}_{\star 8}^{-5/104}\dot{M}_{F4}^{33/104}\rho_p^{-33/52}\ \mathrm{cm} \quad \text{(Stokes)} \end{aligned} \quad (24)$$

When pebbles are weakly coupled with gas the Stokes number $\mathcal{S} \gg 1$, and only a small fraction of pebbles accrete onto an embryo. This inefficiency is considered through the parameter κ in equation (18) as[34]

$$\ln\kappa = -\left(\frac{\mathcal{S}}{\mathcal{S}^*}\right)^{0.65} \tag{25}$$

where the quantity S^* is defined as $\mathcal{S}^* = \min[2, 4\eta^{-3}(m/M_\odot)]$. The above prescription only considers accretion in the midplane of the disk. For bodies on inclined orbits we need to reduce the pebble accretion rate accordingly. Assuming that the pebble density decreases vertically from the midplane as $\exp[-z^2/(2H_p^2)]$ (ref. [30]). Here z is the height of a planet above the midplane, and $H_p = h_p r$ is the pebble scale height (r is the distance to the Sun). The reduction factor in $\dot{m}$ (equation (12)) becomes

$$\int_{z-b}^{z+b} \exp\left(\frac{-Z^2}{2H_p^2}\right) dZ, \tag{26}$$

which can be solved in terms of error functions with proper normalization.

Pebble accretion onto the planet ceases once the planet reaches the so-called pebble isolation mass, which is given by[6]

$$m_p = \frac{1}{2} h^3 M_* \tag{27}$$

Gas envelope accretion. Gas envelope accretion occurs for planets that are massive enough and when the accretion onto the planetary core is low enough for the gas envelope to cool and begin contracting[34]. This occurs when the mass exceeds[35]

$$m = 10\left(\frac{\dot{m}}{10^{-6} M_\oplus\,\mathrm{yr}^{-1}}\right)^{1/4} M_\oplus \tag{28}$$

The gas envelope then collapses and accretes onto the core on the Kelvin–Helmholtz timescale[35]

$$\tau_{KH} = 10^{9\pm1}\left(\frac{M_\oplus}{m}\right)^{3\pm1} \mathrm{yr} \tag{29}$$

We chose the nominal parameter 10^9 yr and an exponent of 3. Gas envelope accretion stops roughly when the Hill radius is roughly equal to the disk scale height. The accretion rate onto the planetary core is then[36]

$$\dot{m}_g = \min\left[\frac{m}{\tau_{KH}}, \dot{M}_* \exp\left(-\frac{m}{m_H}\right)\right] \tag{30}$$

We limit accretion to the Bondi accretion rate, which is given by

$$\dot{m}_{g,B} = \frac{4\pi\rho_g G^2 m^2}{c_s^3} = \frac{2\sqrt{2\pi}\Sigma G^2 m^2}{H^4}\left(\frac{v}{r}\right)^3 \tag{31}$$

where G is the gravitational constant and v is the orbital velocity. In the numerical simulations, we keep track of how much mass in solids and in gas the planet accretes.

Planet migration. The gas disk exerts torques on the embedded planets, which result in a combined effect of radial migration and the damping of the eccentricity and inclination. For low-mass planets, the migration is of type I[37], while massive planets that are able to clear the gas in their vicinity experience type II migration[38]. We follow ref. [39] for computing the torque and the direction of migration in the type I regime. Their formulae are based on ref. [40] for the torque and on refs. [41,42] for the eccentricity damping, including corrections to the damping timescale and corotation torque in the supersonic regime when the eccentricity $e > h$. The normalized torque is[39]

$$\frac{\gamma\Gamma}{\Gamma_0} = \frac{\Gamma_C}{\Gamma_0} F_C + \frac{\Gamma_L}{\Gamma_0} F_L \tag{32}$$

where Γ_C and Γ_L are the corotation and Lindblad torques, respectively[40], and $\Gamma_0 = (M/M_\odot)^2 h^{-2} \Sigma \Omega_K^{-2}$ is a normalization constant. The factors F_L and F_C are defined in refs. [41,42] as

$$\begin{aligned} \ln F_C &= -\frac{e}{e_F} \\ \frac{1}{F_L} &= P_e + \mathrm{sign}(P_e)(0.07\hat{i} + 0.085\hat{i}^4 - 0.08\hat{e}^2\hat{i}^2) \end{aligned} \tag{33}$$

where $e_F = 0.01 + \frac{1}{2}h$, $\hat{e} = e/h$, $\hat{i} = \sin(i)/h$ (e and i are the eccentricity and inclination of the planet), $\mathrm{sign}(x)$ means the sign of quantity x, and

$$P_e = \frac{1 + (0.444\hat{e})^{1/2} + (0.352\hat{e})^6}{1 - (0.495\hat{e})^4} \tag{34}$$

The eccentricity damping timescale $\tau_e = -e/\dot{e}$, where $\dot{e}$ is the rate of decrease of the eccentricity, is[42]

$$\tau_e = 1.282 t_{wav}(1 - 0.14\hat{e}^2 + 0.06\hat{e}^3 + 0.18\hat{e}^2\hat{i}^2) \tag{35}$$

where t_{wav} is the wave timescale, given by[43]

$$t_{wav} = \left(\frac{M_\odot}{M}\right)\left(\frac{M_\odot}{\Sigma r^2}\right) h^4 \Omega_K^{-1} \tag{36}$$

The inclination damping timescale $\tau_i = -i/(\mathrm{d}i/\mathrm{d}t)$ is[42]

$$\tau_i = 1.838 t_{wav}(1 - 0.30\hat{\mathbf{i}}^2 + 0.24\hat{\mathbf{i}}^3 + 0.14\hat{\mathbf{e}}^2\hat{\mathbf{i}}^2) \tag{37}$$

The migration timescale is defined as $\tau_m = -L/\Gamma$, where L and Γ are the angular momentum and the torque, respectively, and is computed as[42]

$$\tau_m = -\frac{t_{wav}\Gamma_0}{h^2\Gamma} \tag{38}$$

For planets in the type II regime, we follow the prescription set out in refs. [12,38]. The migration timescale for such planets is given by

$$\tau_{II} = \frac{r}{3\nu\alpha H^2} \max\left(2r^2, \frac{m_p}{\pi\Sigma}\right) \tag{39}$$

where the first term in parentheses is derived from the typical type II migration rate $\tau_{II} \simeq (2/3)(r/\nu)$ when the disk pushes the planet, and the last term is derived from when the planet pushes the disk and $\tau_{II} \simeq M/\dot{M}_\odot$.

Numerical methods. To study the formation of the giant planets of the Solar System with pebble accretion, we performed a large set of numerical N-body simulations of the Sun and planetary embryos that would eventually turn into the giant planets. We follow the methodology of ref. [12]. These integrations used the Kepler-adapted symplectic N-body code SyMBA[11], a descendant of the original techniques of refs. [44,45]. The code was heavily modified to include the effects of pebble accretion, gas envelope accretion, eccentricity damping and inclination damping from the gas disk, and planet migration through torques induced by the gas disk. These are discussed in detail in ref. [12] and are listed below.

We expect that the accretion of pebbles and gas are small on an orbital timescale, so we have adapted SyMBA as follows. We consider a system made up of the Sun and some number of seed planetary embryos. The planetary embryos, which later become Jupiter, Mars or other planets, are assumed to accrete pebbles and gas. The integration step becomes

$$\mathcal{P}^{\tau/2}\mathcal{M}^{\tau/2}\,\mathcal{I}^{\tau/2}\,\mathcal{D}^{\tau}\,\mathcal{I}^{\tau/2}\,\mathcal{M}^{\tau/2}\mathcal{P}^{\tau/2} \tag{40}$$

where τ is the time step and each term is an operator. The operator $\mathcal{D}$ advances the planets along their osculating Kepler orbits[11] and $\mathcal{I}$ handles the secular interactions between the planets. Both of these operators function according to the regular SyMBA algorithm described in ref. [11] in the democratic heliocentric coordinates (the velocities are barycentric). The other two operators function in heliocentric coordinates before and after coordinate transformation. Specifically, $\mathcal{M}$ generates radial migration and eccentricity and inclination damping, and $\mathcal{P}$ is associated with the accretion of pebbles and gas. Any planetesimals would not feel the $\mathcal{P}$ operators unless they exceed a specific size, and would feel gas drag rather than migration torques for the $\mathcal{M}$ operator.

Second, the accretion of pebbles and gas modifies the Hill spheres and physical radii of the planets, so these need to be updated at regular intervals. Doing so makes the code no longer symplectic, but since the mass of the planets changes slowly enough with time, the changes are adiabatic and the system is approximately symplectic. We computed the planetary radii using the description of ref. [46] for masses below 5 $M_\oplus$ and given by

$$\log\left(\frac{R_p}{3.3\,R_\oplus}\right) = -0.209 + \frac{1}{3}\log\left(\frac{M}{5.5\,M_\oplus}\right) - 0.08\left(\frac{M}{5.5\,M_\oplus}\right)^{0.4} \tag{41}$$

where R_p is the radius of the planetary embryo and $R_\oplus$ is Earth radii. This relation fits Mars, Venus and Earth well. For masses in excess of 5 $M_\oplus$, we used the relation $R_p/R_\oplus = 1.65(M/5\,M_\oplus)^{1/2}$, which is similar to that of ref. [47], but which better fits Jupiter and is acceptable for Uranus and Neptune.

The initial conditions are given in the main text. Initially $\dot{M}_\star = 2.63 \times 10^{-8}\, M_\odot\,\mathrm{yr}^{-1}$ (corresponding to a disk age of 0.5 Myr) and a nominal initial pebble flux of $10^{-4}\, M_\oplus\,\mathrm{yr}^{-1}$ (that is, $\mathcal{F} = 0.1$) and $\alpha = 10^{-3}$. Simulations are run for 4.5 Myr with time steps of 0.01 yr. When $\dot{M}_\star < 10^{-9}\, M_\odot\,\mathrm{yr}^{-1}$, we photoevaporate the disk away in 500 kyr.

Isotopic data. Triple-oxygen isotope values expressed as $\Delta^{17}O_{TFL}$ for terrestrial standards, chondrites, achondrites and Martian meteorites were compiled from data reported in refs. [48–54]; ε^{54}Cr values in terrestrial standards, asteroidal and Martian meteorites are reported in ε notation in refs. [55–64]; ε^{50}Ti values are from refs. [65–67] and ε^{62}Ni from refs. [68–73].

Data availability

The data that support the plots within this paper and other findings of this study are available from the corresponding authors on reasonable request.

Code availability

The source codes and simulation output for the model used in this study are archived at the Earth Life Science Institute of the Tokyo Institute of Technology and are available on request from the corresponding authors. The SyMBA code that our simulations are based on is not in the public domain. It can be requested from its main author H. F. Levison at the Southwest Research Institute.

Received: 28 April 2019; Accepted: 15 November 2019;
Published online: 13 January 2020

References

1. Warren, P. H. Stable-isotopic anomalies and the accretionary assemblage of the Earth and Mars: a subordinate role for carbonaceous chondrites. *Earth Planet. Sci. Lett.* **311**, 93–100 (2011).
2. Kruijer, T. S., Burkhardt, C., Budde, G. & Kleine, T. Age of Jupiter inferred from the distinct genetics and formation times of meteorites. *Proc. Natl Acad. Sci.* **114**, 6712–6716 (2017).
3. Alibert, Y. et al. The formation of Jupiter by hybrid pebble–planetesimal accretion. *Nat. Astron.* **2**, 873–877 (2018).
4. Huang, J. et al. The Disk Substructures at High Angular Resolution Project (DSHARP). III. Spiral structures in the millimeter continuum of the Elias 27, IM Lup, and WaOph 6 disks. *Astrophys. J.* **869**, L43 (2018).
5. Lambrechts, M. & Johansen, A. Rapid growth of gas-giant cores by pebble accretion. *Astron. Astrophys.* **544**, A32 (2012).
6. Lambrechts, M., Johansen, A. & Morbidelli, A. Separating gas-giant and ice-giant planets by halting pebble accretion. *Astron. Astrophys.* **572**, A35 (2014).
7. Ida, S., Guillot, T. & Morbidelli, A. The radial dependence of pebble accretion rates: a source of diversity in planetary systems. I. Analytical formulation. *Astron. Astrophys.* **591**, A72 (2016).
8. Ormel, C. W. & Liu, B. Catching drifting pebbles. II. A stochastic equation of motion for pebbles. *Astron. Astrophys.* **615**, A178 (2018).
9. Sato, T., Okuzumi, S. & Ida, S. On the water delivery to terrestrial embryos by ice pebble accretion. *Astron. Astrophys.* **589**, A15 (2016).
10. Morbidelli, A. et al. Fossilized condensation lines in the Solar System protoplanetary disk. *Icarus* **267**, 368–376 (2016).
11. Duncan, M. J., Levison, H. F. & Lee, M. H. A multiple time step symplectic algorithm for integrating close encounters. *Astron. J.* **116**, 2067–2077 (1998).
12. Matsumura, S., Brasser, R. & Ida, S. *N*-body simulations of planet formation via pebble accretion. I. First results. *Astron. Astrophys.* **607**, A67 (2017).
13. Wang, H. et al. Lifetime of the solar nebula constrained by meteorite paleomagnetism. *Science* **355**, 623–627 (2017).
14. Johansen, A., Ida, S. & Brasser, R. How planetary growth outperforms migration. *Astron. Astrophys.* **622**, A202 (2019).
15. Woo, J. M. Y., Brasser, R., Matsumura, S., Mojzsis, S. J. & Ida, S. The curious case of Mars' formation. *Astron. Astrophys.* **617**, A17 (2018).
16. Levison, H. F., Kretke, K. A., Walsh, K. J. & Bottke, W. F. Growing the terrestrial planets from the gradual accumulation of submeter-sized objects. *Proc. Natl Acad. Sci.* **112**, 14180–14185 (2015).
17. Marty, B. The origins and concentrations of water, carbon, nitrogen and noble gases on Earth. *Earth Planet. Sci. Lett.* **313**, 56–66 (2012).
18. Dauphas, N. The isotopic nature of the Earth's accreting material through time. *Nature* **541**, 521–524 (2017).
19. Kretke, K. A. & Lin, D. N. C. Grain retention and formation of planetesimals near the snow line in MRI-driven turbulent protoplanetary disks. *Astrophys. J.* **664**, L55–L58 (2007).
20. Vorobyov, E. I., Akimkin, V., Stoyanovskaya, O., Pavlyuchenkov, Y. & Liu, H. B. Early evolution of viscous and self-gravitating circumstellar disks with a dust component. *Astron. Astrophys.* **614**, A98 (2018).
21. van der Marel, N., Williams, J. P. & Bruderer, S. Rings and gaps in protoplanetary disks: planets or snowlines? *Astrophys. J.* **867**, L14 (2018).
22. Pinilla, P. et al. Trapping dust particles in the outer regions of protoplanetary disks. *Astron. Astrophys.* **538**, A114 (2012).
23. van der Marel, N. et al. A concentration of centimeter-sized grains in the Ophiuchus IRS 48 dust trap. *Astrophys. J.* **810**, L7 (2015).
24. Pinilla, P., Flock, M., Ovelar, M. & Birnstiel, T. Can dead zones create structures like a transition disk? *Astron. Astrophys.* **596**, A81 (2016).
25. Desch, S. J., Kalyaan, A. & Alexander, C. M. O'D. The effect of Jupiter's formation on the distribution of refractory elements and inclusions in meteorites. *Astrophys. J. Suppl.* **238**, A11 (2018).
26. Andrews, S. M. et al. Ringed substructure and a gap at 1 au in the nearest protoplanetary disk. *Astrophys. J.* **820**, L40 (2016).
27. Long, F. et al. Gaps and rings in an ALMA survey of disks in the Taurus star-forming region. *Astrophys. J.* **869**, A17 (2018).
28. Morbidelli, A., Tsiganis, K., Crida, A., Levison, H. F. & Gomes, R. Dynamics of the giant planets of the Solar System in the gaseous protoplanetary disk and their relationship to the current orbital architecture. *Astron. J.* **134**, 1790–1798 (2007).
29. Kanagawa, K. D. et al. Impacts of dust feedback on a dust ring induced by a planet in a protoplanetary disk. *Astrophys. J.* **868**, A48 (2018).
30. Levison, H. F., Kretke, K. A. & Duncan, M. J. Growing the gas-giant planets by the gradual accumulation of pebbles. *Nature* **524**, 322–324 (2015).
31. Shakura, N. I. & Sunyaev, R. A. Black holes in binary systems. Observational appearance. *Astron. Astrophys.* **24**, 337–355 (1973).
32. Hartmann, L., Calvet, N., Gullbring, E. & D'Alessio, P. Accretion and the evolution of T Tauri disks. *Astrophys. J.* **495**, 385–400 (1998).
33. Garaud, P. & Lin, D. N. C. The effect of internal dissipation and surface irradiation on the structure of disks and the location of the snow line around Sun-like stars. *Astrophys. J.* **654**, 606–624 (2007).
34. Ormel, C. W. & Klahr, H. H. The effect of gas drag on the growth of protoplanets. Analytical expressions for the accretion of small bodies in laminar disks. *Astron. Astrophys.* **520**, A43 (2010).
35. Ikoma, M., Nakazawa, K. & Emori, H. Formation of giant planets: dependences on core accretion rate and grain opacity. *Astrophys. J.* **537**, 1013–1025 (2000).
36. Ida, S., Lin, D. N. C. & Nagasawa, M. Toward a deterministic model of planetary formation. VII. Eccentricity distribution of gas giants. *Astrophys. J.* **775**, 42 (2013).
37. Tanaka, H., Takeuchi, T. & Ward, W. R. Three-dimensional interaction between a planet and an isothermal gaseous disk. I. Corotation and Lindblad torques and planet migration. *Astrophys. J.* **565**, 1257–1274 (2008).
38. Lin, D. N. C. & Papaloizou, J. C. B. On the tidal interaction between protoplanets and the protoplanetary disk. III. Orbital migration of protoplanets. *Astrophys. J.* **309**, 846–857 (1986).
39. Coleman, G. A. L. & Nelson, R. P. On the formation of planetary systems via oligarchic growth in thermally evolving viscous discs. *Mon. Not. R. Astron. Soc.* **445**, 479–499 (2014).
40. Paardekooper, S.-J., Baruteau, C. & Kley, W. A torque formula for non-isothermal type I planetary migration. II. Effects of diffusion. *Mon. Not. R. Astron. Soc.* **410**, 293–303 (2011).
41. Fendyke, S. M. & Nelson, R. P. On the corotation torque for low-mass eccentric planets. *Mon. Not. R. Astron. Soc.* **437**, 96–107 (2014).
42. Cresswell, P. & Nelson, R. P. Three-dimensional simulations of multiple protoplanets embedded in a protostellar disc. *Astron. Astrophys.* **482**, 677–690 (2008).
43. Tanaka, H. & Ward, W. R. Three-dimensional interaction between a planet and an isothermal gaseous disk. II. Eccentricity waves and bending waves. *Astrophys. J.* **602**, 388–395 (2004).
44. Wisdom, J. & Holman, M. Symplectic maps for the *N*-body problem. *Astron. J.* **102**, 1528–1538 (1991).
45. Kinoshita, H., Yoshida, H. & Nakai, H. Symplectic integrators and their application to dynamical astronomy. *Celest. Mech. Dyn. Astron.* **50**, 59–71 (1991).
46. Seager, S., Kuchner, M., Hier-Majumder, C. A. & Militzer, B. Mass–radius relationships for solid exoplanets. *Astrophys. J.* **669**, 1279–1297 (2007).
47. Lissauer, J. J. et al. Architecture and dynamics of Kepler's candidate multiple transiting planet systems. *Astrophys. J. Suppl.* **197**, A8 (2011).
48. Clayton, R. N. & Mayeda, T. K. Oxygen isotopes in eucrites, shergottites, nakhlites, and chassignites. *Earth Planet. Sci. Lett.* **62**, 1–6 (1983).
49. Clayton, R. N. & Mayeda, T. K. Oxygen isotope studies of achondrites. *Geochim. Cosmochim. Acta* **60**, 1999–2017 (1996).
50. Franchi, I. A., Wright, I. P., Sexton, A. S. & Pillinger, C. T. The oxygen-isotopic composition of Earth and Mars. *Meteorit. Planet. Sci.* **34**, 657–661 (1999).
51. Rubin, A. E. et al. Los Angeles: the most differentiated basaltic Martian meteorite. *Geology* **28**, 1011–1014 (2000).
52. Mittlefehldt, D. W., Clayton, R. N., Drake, M. J. & Righter, K. Oxygen isotopic composition and chemical correlations in meteorites and the terrestrial planets. *Rev. Mineral. Geochem.* **68**, 399–428 (2008).
53. Agee, C. B. et al. Unique meteorite from early Amazonian Mars: water-rich basaltic breccia Northwest Africa 7034. *Science* **339**, 780–785 (2013).
54. Wittmann, A. et al. Petrography and composition of Martian regolith breccia meteorite Northwest Africa 7475. *Meteorit. Planet. Sci.* **50**, 326–352 (2015).

55. Trinquier, A., Birck, J.-L. & Allegre, C. J. Widespread ^{54}Cr heterogeneity in the inner Solar System. *Astrophys. J.* **655**, 1179–1185 (2007).
56. Trinquier, A., Birck, J.-L., Allegre, C. J., Göpel, C. & Ulfbeck, D. ^{53}Mn-^{53}Cr systematics of the early Solar System revisited. *Geochim. Cosmochim. Acta* **72**, 5146–5163 (2008).
57. Qin, L., Alexander, C. M. O'D., Carlson, R. W., Horan, M. F. & Yokoyama, T. Contributors to chromium isotope variation of meteorites. *Geochim. Cosmochim. Acta* **74**, 1122–1145 (2010).
58. Petitat, M., Birck, J.-L., Luu, T. H. & Gounelle, M. The chromium isotopic composition of the ungrouped carbonaceous chondrite Tagish Lake. *Astrophys. J.* **736**, 23–31 (2011).
59. Yamakawa, A. & Yin, Q.-Z. Chromium isotopic systematics of the Sutter's Mill carbonaceous chondrite: implications for isotopic heterogeneities of the early Solar System. *Meteorit. Planet. Sci.* **49**, 2118–2127 (2014).
60. Shukolyukov, A. & Lugmair, G. W. Manganese-chromium isotope systematics of carbonaceous chondrites. *Earth Planet. Sci. Lett.* **250**, 200–213 (2006).
61. Yamashita, K., Maruyama, S., Yamakawa, A. & Nakamura, E. ^{53}Mn-^{53}Cr chronometry of CB chondrites: evidence for uniform distribution of ^{53}Mn in the early Solar System. *Astrophys. J.* **728**, A165 (2010).
62. Larsen, K. K. et al. Evidence for magnesium isotope heterogeneity in the solar protoplanetary disk. *Astrophys. J. Lett.* **735**, L37 (2011).
63. Göpel, C. & Birck, J.-L. Mn/Cr systematics: a tool to discriminate the origin of primitive meteorites? *Geochim. Cosmochim. Acta* **74**, A348 (2010).
64. Qin, L. et al. The chromium isotopic composition of Almahata Sitta. *Meteorit. Planet. Sci.* **45**, 1771–1777 (2010).
65. Trinquier, A. et al. Origin of nucleosynthetic isotope heterogeneity in the solar protoplanetary disk. *Science* **324**, 374–377 (2009).
66. Zhang, J., Dauphas, N., Davis, A. M., Leya, I. & Fedkin, A. The proto-Earth as a significant source of lunar material. *Nat. Geo.* **5**, 251–255 (2012).
67. Zhang, J., Dauphas, N., Davis, A. M. & Pourmand, A. A new method for MC-ICPMS measurement of titanium isotopic composition: identification of correlated isotope anomalies in meteorites. *J. Anal. At. Spectrom.* **26**, 2197–2205 (2011).
68. Regelous, M., Elliott, T. & Coath, C. D. Nickel isotope heterogeneity in the early Solar System. *Earth Planet. Sci. Lett.* **272**, 330–338 (2008).
69. Steele, R. C. J., Coath, C. D., Regelous, M., Russell, S. & Elliott, T. Neutron-poor nickel isotope anomalies in meteorites. *Astrophys. J.* **758**, A59 (2012).
70. Steele, R. C. J., Elliott, T., Coath, C. D. & Regelous, M. Confirmation of mass-independent Ni isotopic variability in iron meteorites. *Geochim. Cosmochim. Acta* **75**, 7906–7925 (2011).
71. Tang, H. & Dauphas, N. Abundance, distribution, and origin of ^{60}Fe in the solar protoplanetary disk. *Earth Planet. Sci. Lett.* **359**, 248–263 (2012).
72. Tang, H. & Dauphas, N. ^{60}Fe-^{60}Ni chronology of core formation in Mars. *Earth Planet. Sci. Lett.* **390**, 264–274 (2014).
73. Dauphas, N. et al. Iron-60 evidence for early injection and efficient mixing of stellar debris in the protosolar nebula. *Astrophys. J.* **686**, 560–569 (2008).

Acknowledgements

We thank S. Matsumura for the pebble accretion code, B. Bitsch for sharing the location of gas pressure maxima outwards of planets and E. Vorobyov for pointing out dust pile-up in the inner disk. R.B. acknowledges financial assistance from the Japan Society for the Promotion of Science (JSPS) International Joint Research Fund (JP17KK0089) and JSPS Shingakujutsu Kobo (JP19H05071).

Author contributions

Both authors devised the study and wrote the manuscript. R.B. ran and analysed the dynamical simulations. S.J.M. compiled the cosmochemical isotopic database.

Competing interests

The authors declare no competing interests.

Additional information

Extended data is available for this paper at https://doi.org/10.1038/s41550-019-0978-6.

Correspondence and requests for materials should be addressed to R.B. or S.J.M.

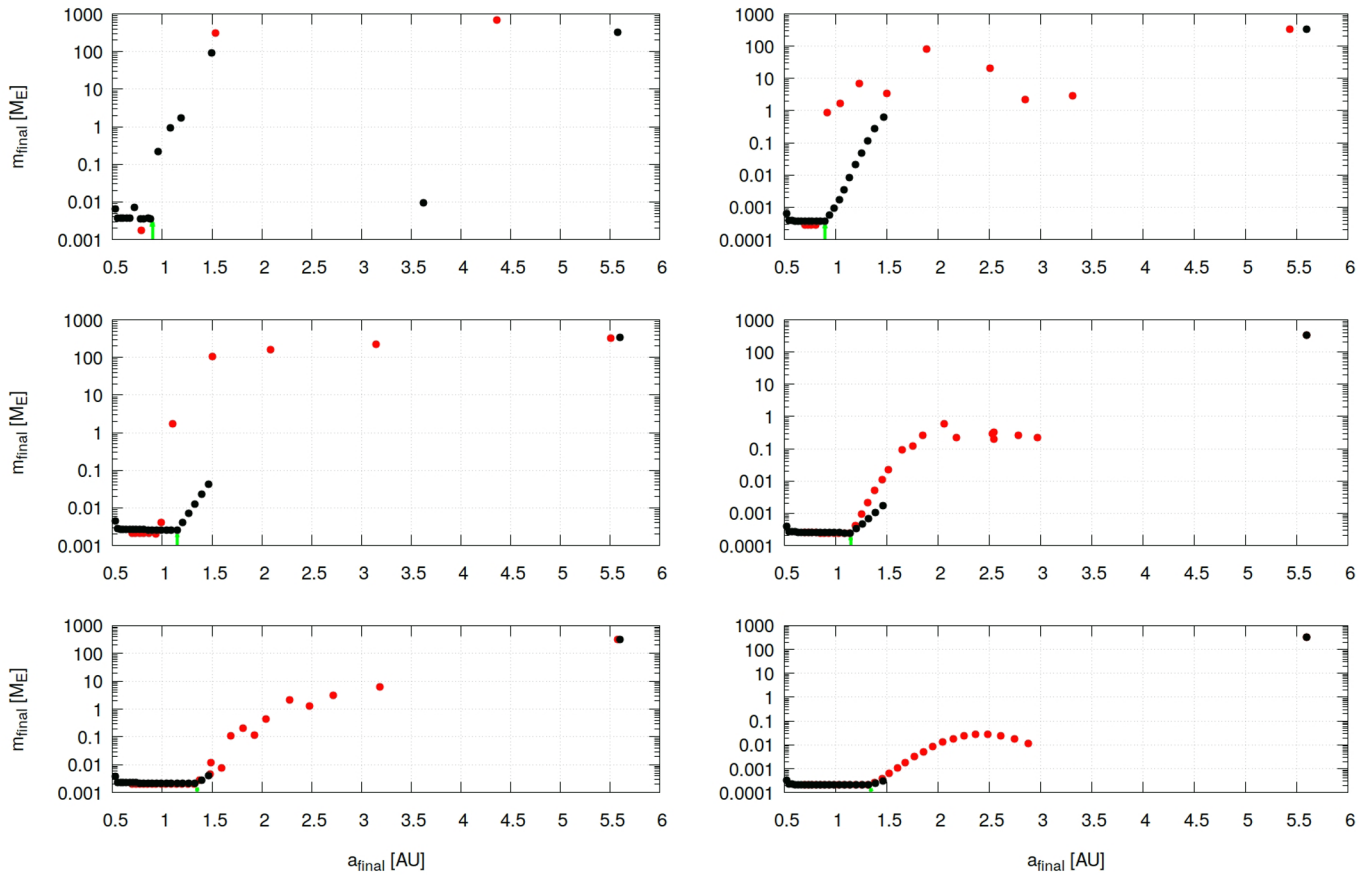

Extended Data Fig. 1 | Additional Embryo Simulations. Additional simulations with multiple seed planets, distributed between 0.5 au and either 1.5 au or 3.5 au. In each simulation all the seeds initially have the same mass (either 10^{-3} or 10^{-4} $M_{\oplus}$), but we vary this mass between simulations. Initial disk temperature at 1 au is either 200 K, 250 K or 300 K. The top row has an initial disc temperature of 200 K, middle row 250 K and bottom row 300 K. Red dots are for simulations with embryos between 0.5 au and 3.5 au, black for embryos terminating at 1.5 au. The left column has embryos with initial mass 10^{-3} $M_{\oplus}$, the right column with 10^{-4} $M_{\oplus}$. In all cases, placing embryos in the asteroid belt overshoots the mass in that region, though a truncation near 2 au may be viable to explore in future work.

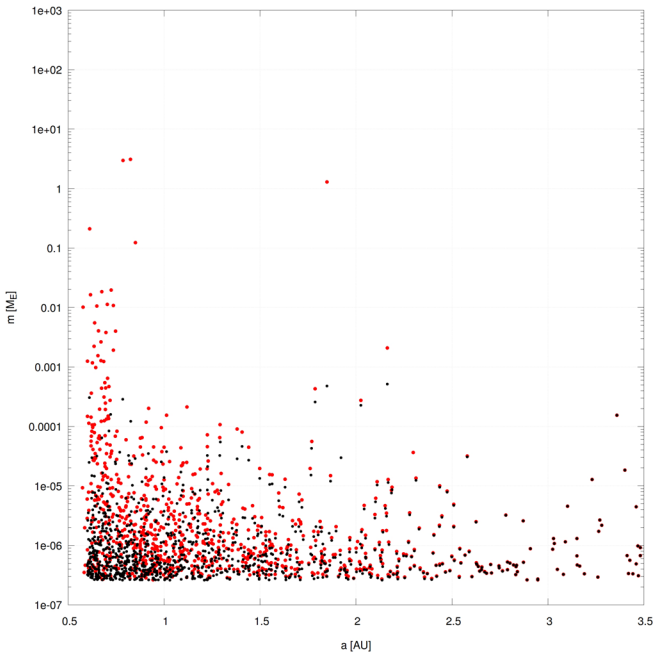

Extended Data Fig. 2 | Planetesimal accretion of pebbles without Jupiter. Initial (black) and final (red) masses and semi-major axes of a swarm of planetesimals with diameters from 100 km to 2000 km without Jupiter. The planetesimals have with a cumulative size-frequency distribution $N(>D) \propto D^{-5/2}$ and initial density 2000 kg m^{-3}; this is a top-heavy distribution where most of the mass is in the large bodies. The disk temperature at 1 au was set to 200 K. In the innermost portion of the planetesimal disk bodies accrete >50% of their own mass in pebbles. The growth is inside-out.

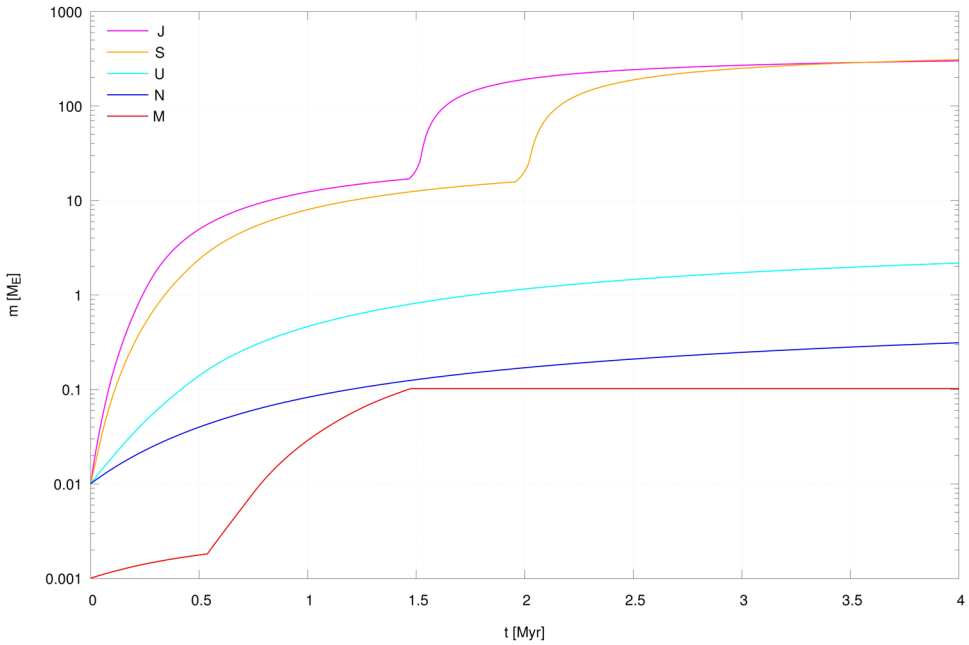

Extended Data Fig. 3 | Growth tracks of Jupiter, Saturn, Uranus and Neptune with pebble accretion. Evolution of the mass of Jupiter, Saturn, Uranus, Neptune and Mars analogue as a function of time when growing by pebble accretion for nominal pebble flux and growth of Jupiter consistent with cosmochemical ages. The original disk temperature at 1 au is 250 K. No migration was included.

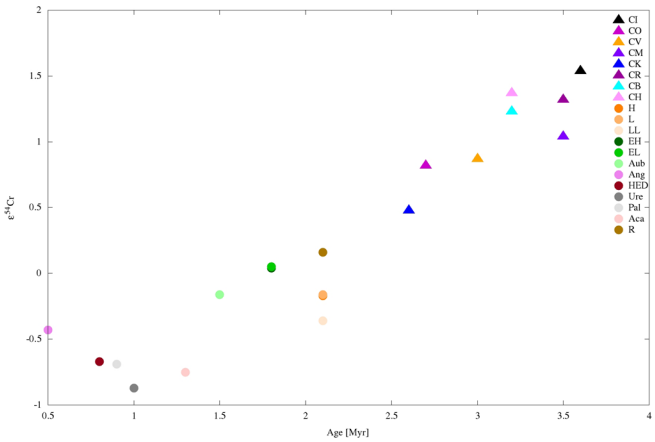

Extended Data Fig. 4 | Meteorite parent body model formation ages. Model formation age of chondrite parent bodies versus isotopic anomalies in chromium-54 (N. Sugiura and W. Fujiya, *Meteorit. Planet. Sci.* **49**, 772–787; 2014). Bodies in the inner solar system tend to form earlier than bodies in the outer solar system.